Large Eddy Simulation of a Heaving Wing on the Cusp of Transition to Turbulence

Charles E. Badoe*,†, Zheng-Tong Xie* and Neil D. Sandham*

* *Aerodynamics and Flight Mechanics Group, Faculty of Engineering and the Environment, University of Southampton, Southampton, SO17 1BJ, United Kingdom.*
† *Corresponding author: ceb1r14@soton.ac.uk*

Abstract

Simulations of the flow over a heaving NACA 0012 wing are conducted to study the separated flow phenomena for a pre-stall and post-stall wing condition. An extensively validated high fidelity large-eddy simulation (LES) approach is used to examine the unsteady aerodynamic loads and flow structures at Reynolds number $Re_c = 2 \times 10^4$ based on the chord. We consider reduced frequencies of k=0.47 and 0.94 for a chord-normalized peak-to-peak amplitude of A/c=0.5 and angles of attack of 5° and 15°, representing pre-stall and post-stall conditions respectively. Comparison to experiment shows good agreement for the phase-averaged lift, drag and moments of the heaving wing. Characteristic phenomena of dynamic stall are analysed with emphasis on the leading edge vortex (LEV) development. A series of instantaneous spanwise vorticity plots show significant spanwise perturbations in the reverse flow region that develops over the suction surface during the start of the downstroke, giving rise to instabilities in the detached shear layer. The instabilities give rise to the first occurrence of turbulence near the wing surface at the leading edge.

Keywords: Dynamic stall, Large-eddy simulations, Oscillating wing, Transition, Instability

1. Introduction

The unsteady aerodynamics of oscillating wings has received much attention in recent years. A wide range of studies, including those of [1-6] has increased our knowledge of the unsteady flow patterns and transient effects, including flow instabilities and vortex shedding, primarily from a two-dimensional perspective. These studies have been largely driven by interest in, for example, natural flyers, micro air vehicles (MAV) and other unmanned aerial vehicles (UAVs). These vehicles operate mostly at low airspeed and low Reynolds number, typically Reynolds number magnitude of $O(10^4 - 10^5)$ [7].

The flow over the wings of these vehicles at this Reynolds number range is very complicated and can experience a dynamic stall behaviour, which exhibits large hysteresis on the lift and moment when the time varying angle of incidence goes beyond its static stall angle, due to the unsteady wing motion [8-9]. This makes them very challenging to model numerically. It has been found [10] that the leading edge vortex (LEV) plays a critical role in the lift enhancement. In static wing aerodynamics, near the stall angle the flow is highly unsteady and separated. Measurements [11-17] have shown that the unsteady flow has a low coherency in the spanwise direction, even for a two-dimensional geometry.

In order to improve the understanding of oscillating wing aerodynamics, a number of studies have been carried out to investigate the complex wing motion with simple kinematics such as in pure pitching or heaving motion using unsteady Reynolds-averaged Navier-Stokes (RANS) methods [18-21]. Most of this research has shown that RANS methods are not sufficient to predict such a time-dependent flow structure. For example, when the frequency of a periodically-oscillating wing is increased, it induces large shed vortices and downstream vorticity [22]. Wang et al.[21] showed that RANS methodologies are not suitable to predict such flow details and suggested that advanced approaches such as direct numerical simulation (DNS) or large eddy simulation (LES) should be used to capture the details of such flows.

The majority of the DNS and LES computational studies and especially with heaving motion tend to focus on three-dimensional wings, near-wake structures or spanwise vortical structures at high reduced frequency ($k \geqslant 2.0$) and low amplitude ($A/c \leqslant 0.1$). Despite the valuable insight from these studies, there is still a gap in the unsteady wing behaviour at much lower reduced frequency and higher amplitude [22-24]. This is because the large variations of transition points on the suction-surface of an airfoil during the pitching or heaving cycle require very large computational resources to capture and understand such flow detail. There are open questions about the effect of transition on the wing motion, for example, the stability of the leading-edge vortex within these conditions and the first occurrence (as well as phase angle) of turbulence on the wing surface. The work of [25] on two and three-dimensional pitching and plunging flat plates at Reynolds numbers $O(10^4)$ and reduced frequency $k = 0.2$, considering shallow stall and a deep stall motion, showed massive leading-edge separation at the sharp leading edge of the flat plate. Similar observations were also made by [26] on a heaving flat plate.

Others such as [27-29] also used LES method to study the unsteady flow over a pitching wing. The investigations of [27] were made for $k = 0.25$-1.0 and $Re_c = 135{,}000$. Pitching was achieved by using a dynamic mesh that deformed the cells each time step, allowing the wing boundary to move within the domain. The approach was able to predict the trends in the coefficients of lift, drag and moments compared with the experimental data. Spanwise vorticity components and instantaneous streamlines also compared well with experiments. There was little information on the transition of the motion since the main focus of their work was the effect of the aerodynamic forces on the pitching wing.

In the current contribution, we use a similar approach to [27] to examine the physics behind the dynamic stall of a heaving wing (considering low reduced frequency and higher amplitude) at Reynolds number $O(10^4)$ where effect of transition is unclear. The aim is to (i) assess the performance of the LES approach for the prediction of the aerodynamic loads through comparison with experimental water tunnel data, and (ii) analyse any flow instabilities at the leading edge during a heaving cycle and the role of these instabilities in separation bubble transition. The intention is also to identify the first occurrence of unsteadiness at the wing surface. The Reynolds number influence on the LEV is also studied.

The remainder of this paper is organised as follows: In §2 we present the mathematical and numerical details of the LES, while the sensitivity of the LES methodology is analysed and explained in detail in §3. In §4 the results are validated against experimental water tunnel data and significant features of dynamic stall are presented. The section also provides insight into the variations in transition during the heaving cycle. §5 provides insight into the influence of Reynolds number on the flow structure and aerodynamic loads. Summary and concluding remarks are presented in §6.

2. Numerical Methodology

2.1. Governing equations

For the heaving manoeuvre, the governing equations are the unsteady filtered Navier-Stokes equations. Within the assumption of an incompressible fluid and by denoting the filtering operation with an overbar, the set of equations may be written in the form:

$$\frac{\partial \overline{u}_i}{\partial x_i} = 0 \tag{1}$$

$$\frac{\partial \overline{u}_i}{\partial t} + \frac{\partial \overline{u}_i \overline{u}_j}{\partial x_j} = -\frac{1}{\rho}\frac{\partial \overline{p}}{\partial x_i} + \frac{\partial}{\partial x_j}\left(\nu \frac{\partial \overline{u}_i}{\partial x_j} - \tau^r_{ij}\right), \tag{2}$$

where τ^r_{ij} is the non-linear subgrid-scale (SGS) stress tensor which should be modelled. Thus, ghanaweb

$$\tau^r_{ij} = \overline{u_i u_j} - \overline{u}_i \overline{u}_j \tag{3}$$

$$\tau^r_{ij} = -2\nu_t \overline{S}_{ij} + \frac{1}{3}\delta_{ij}\tau_{kk}, \tag{4}$$

where the Kronecker delta $\delta_{ij} = 1$ for $i = j$, otherwise $\delta_{ij} = 0$; ν_t is the SGS eddy viscosity and $\overline{S}_{ij}$ is the rate-of-strain tensor for the resolved scale defined by

$$\overline{S}_{ij} = \frac{1}{2}\left(\frac{\partial \overline{u}_i}{\partial x_j} + \frac{\partial \overline{u}_j}{\partial x_i}\right). \tag{5}$$

Both the mixed time-scale (MTS) model of [30] and the wall adapting local eddy-viscosity (WALE) model of [31] have been used. The advantages of both models are that the eddy viscosity goes naturally to zero in the wall region, so neither constant adjustments nor damping functions are needed to compute wall bounded flows. Both models have also been credible when applied to transitional flow past wings which is one of the key aspects of the present application. For example, there have been applications to a NACA0015 at $\alpha = 11°$, $Re_c = 1.0 \times 10^6$ [21] a NACA0012 at $\alpha = 10°$, $Re_c = 13.5 \times 10^4$[27-28] and a NACA0012 at $\alpha = 5°$, $Re_c = 5 \times 10^4$ [32].

2.2. Applied LES-CFD solver and dynamic mesh

The LES have been carried carried out using OpenFOAM version 2.3.0. A second order implicit scheme was used for the temporal discretization and the bounded second order (Gamma) scheme, with a factor $\Gamma = 0.25$ [33] was used for the convection term. The time step $\triangle t U_\infty / c = 8.0 \times 10^{-4}$ corresponds to 4000 time steps per cycle. The pimpleDyMFoam solver in OpenFOAM was used, which is a transient solver for incompressible flow on a moving mesh utilising the PIMPLE (merged PISO-SIMPLE) algorithm. The PIMPLE algorithm includes both under relaxation and velocity correction and is mainly used for transient flows, but without the same Courant number constraints of the PISO algorithm. The number of outer iterations was set to two and the number of pressure corrections was set to three. In the pimpleDyMFoam solver, nodal locations are recalculated with each time step according to a prescribed boundary motion and diffusivity γ. Then, once the vertex velocity, u_v is prescribed, it is interpolated to obtain the local boundary velocity, u_b. The diffusivity γ then defines how the vertex motion is diffused to prevent high mesh deformation close to the boundary according to

$$\bigtriangledown \cdot (\gamma \bigtriangledown u_v) = 0. \tag{6}$$

Once the boundary conditions are calculated from the previous boundary motion of a moving wall, the vertex position at time $n+1$ is updated using the vertex velocity, u_v

$$x^{n+1} = x^n + u_v \Delta t. \tag{7}$$

For static computations involving no mesh deformation, γ is kept constant, however in dynamic computations involving mesh deformation, γ is varied to maintain high mesh quality around the moving geometry. Jasak and Tukovic [34] highlighted the importance of the diffusivity on the mesh quality at the trailing edge of a moving geometry. They found that the mesh quality is superior when a quadratic diffusivity is used as compared to other types such as linear and exponential. As a result, the quadratic diffusivity defined in equation 8 is used in this work.

$$\gamma = \frac{1}{l^2}, \tag{8}$$

where l is the cell centre distance to the nearest selected boundary.

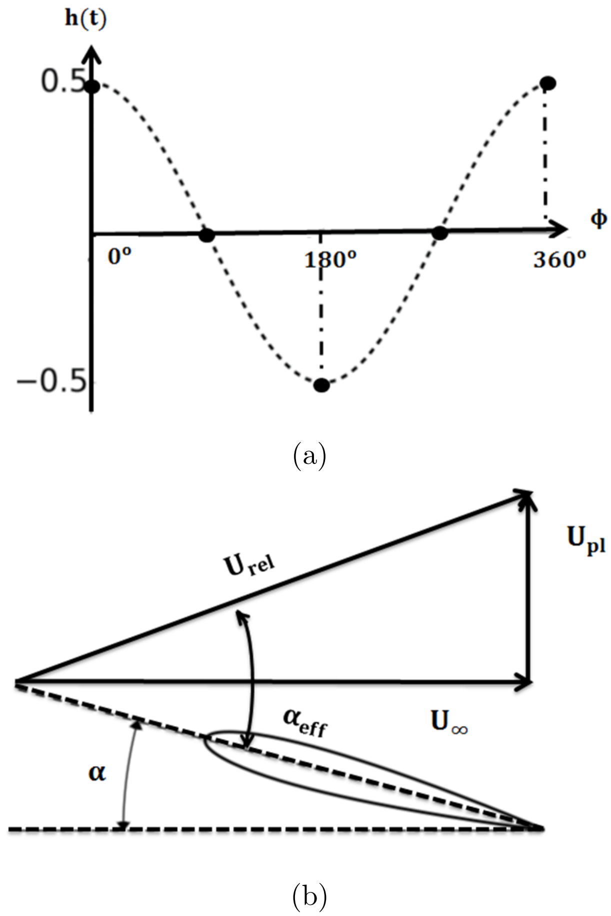

Figure 1: (a) Illustration of heaving motion, where the phase angle $0^\circ \leq \phi \leq 360^\circ$ (b) Effective angle of attack definition: $\alpha_{eff}(t) = \alpha + \tan^{-1}(U_{pl}(t)/U_\infty)$ where U_{pl} denotes the plunge velocity, U_{rel} the relative velocity and α is the geometric angle of attack. Note: wing vertical position $h(t) = A/2 \cos 2\pi\text{ft}$.

2.3. Simulation parameters and grid generation

The wing section considered in the present study has a NACA 0012 profile with chord $c = 0.0627$m and was modified to include a sharp trailing edge. The wing section has been the subject of a recent experimental water tunnel investigation [35]. Unsteady and phase-averaged computations were conducted with reduced frequencies $k = 0.47$ and 0.94 (where $k = \pi \; fc/U_\infty$ and f is frequency, c is the airfoil chord and U_∞ is the inflow velocity) and peak-to-peak amplitude $A/c = 0.5$. Two different angles of attack were con-

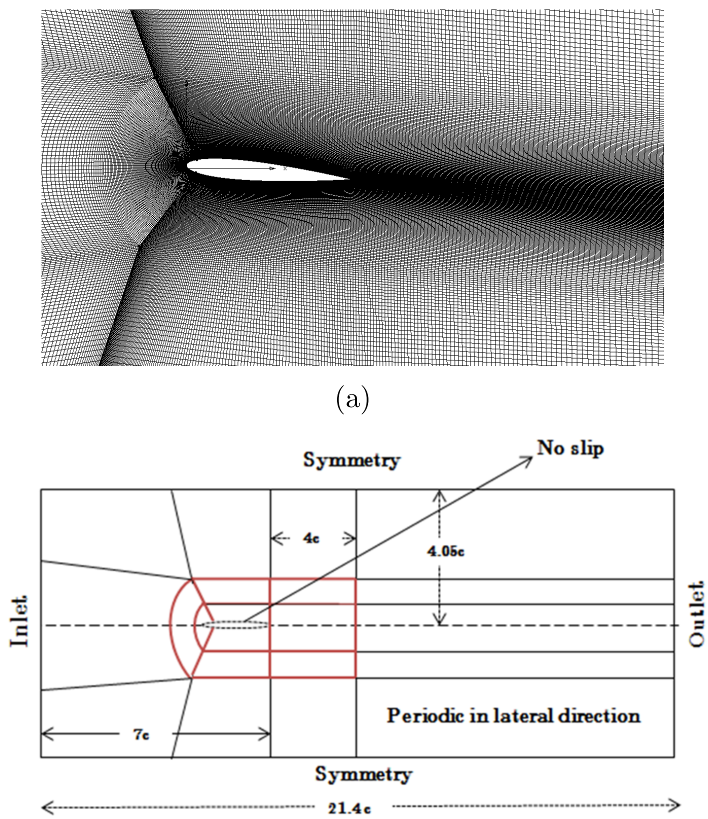

(a)

(b)

Figure 2: (a) Mesh topology (b) Sketch of the domain including applied boundary conditions (not to scale).

sidered, namely $\alpha = 5°$ and $\alpha = 15°$. The plunging motion follows a cosine function (see Figure 1). A sketch of the computational domain created using Pointwise version 16 is shown in Figure 2. The set-up matches experimental water tunnel conditions in the axial and lateral directions. A C-type grid was adopted close to the wing surface. Away from the wing surface, an H-type grid was used. Grid points were concentrated around the wing boundary layer to capture the transition process. The domain was extruded in the spanwise direction by $0.25c$ and had a uniform spacing of about 30 to 60 cells, aiming to provide $5 \leq \triangle z^+ \leq 10$ over the wing surface. This span was selected based on a spanwise sensitivity study, as described in section 3. For the wall normal spacing, the mesh was designed to satisfy a $y^+ \leq 1$

criterion at the wall. An approximate $\triangle x^{+} \leq 10$ was also achieved on the wing surface. In the near wake region (from the wing trailing edge to a distance of 4 chords) the spacing was kept uniform and an aspect ratio of 1 was maintained to capture the anticipated near wake vortices. To avoid building separate grids for each angle of attack and also to maintain the strict LES requirements, the blocks surrounding the wing section (denoted in red in Figure 2b), together with the wing, were rotated about the quarter chord to the desired neutral angle of attack, with the vertices of those blocks adjusted accordingly to generate low skewed cells and to maintain a good quality mesh in the boundary layer and wake region. Boundary conditions include no-slip and symmetry conditions at the wall and the two lateral boundaries respectively. Periodic conditions were also imposed in the spanwise di1.4rection. Heaving computations were started from a previously simulated static condition (static cases were computed for about 10 chord flow pasts) and then run for about 7 cycles. Data was processed from the third cycle onwards.

3. Sensitivity Studies

3.1. Grid resolution effects

Three different grids were used to provide insight into the impact of grid spacing on the overall prediction of the aerodynamic loads. The grids, labelled G1,G2 and G3 were generated based on the same geometry definition by a systematic $\sqrt{2}$ refinement of the reference structured block-grid. The number of points was varied in all three directions simultaneously. The grid system used for the analysis is shown in Table 1, where the computational domain size is normalised by the wing chord c and U, H, W and Z are the upstream length, domain height, wake length and span length respectively. N_{AU} is the number of grid points on the wing upper surface, N_{AL} is the number of grid points on the wing lower surface and $\Delta z/c$ is the spanwise spacing. An illustration of the grid generated on the wing is also shown in Figure 2a for grid G2. The effect of the grid resolution on the lift and drag coefficient is shown in Figure 3 and Table 2. Data in Figure 3 was taken after the third cycle because it was found that the hysteresis loop from the successive cycles in general closely matched that of the third cycle, as shown in the time history plots of the aerodynamic loads in Figure 4. From the grid resolution study it was found that grid resolution had little effect during the wing's downward displacement (i.e. the increasing lift side of the hysteresis loop in Figure 3).There were, however, some quantitative differences during the wing's upwards displacement. This is because of the unsteadiness of the flow structure within these regions, where the prominent elements in the flow are the separated shear layer emanating from the leading edge and the development of the trailing edge vortex (TEV). It is crucial that the mesh is fine enough to capture these unsteady flow structures. The results on the coarse grid G1 (see Table 2) deviate from the medium grid G2 by about 1% and fine grid G3 by about 3%, probably due to the fact that the spanwise spacing of $\Delta z/c$=30 is not enough to resolve the details. Although G2 and G3 (with about 1% difference between them) agree well with each other, there are still some minor differences, which are of the order of the cycle-to-cycle variations.

Table 1: Grid and domain parameters, $Re_c = 2 \times 10^4$, $\alpha = 5°$, $k = 0.94$ and $A/c = 0.5$

$Mesh$	$Size$	N_{AU}	N_{AL}	$\Delta z/c$	$U[c]$	$W[c]$	$H[c]$	$Z[c]$
G1	456×176×30	176	176	0.0083	7.0	14.4	4.05	0.25
G2	645×249×43	249	249	0.0058	7.0	14.4	4.05	0.25
G3	912×352×60	352	352	0.0041	7.0	14.4	4.05	0.25

Table 2: Grid sensitivity analysis, $Re_c = 2 \times 10^4$, $\alpha = 5°$, $k = 0.94$ and $A/c = 0.5$

$Mesh$	Δx^+	Δz^+	$y1^+$	$C_{L_{ave}}$	$C_{D_{ave}}$
G1	10	10	4	0.691	-0.0458
G2	8	8	1	0.701	-0.0416
G3	6	5	0.64	0.709	-0.0402

NB: $C_{L_{Exp}} = 0.758$

3.2. Effect of Subgrid model

Two different subgrid models were used to investigate the effect of the subgrid model on the computed aerodynamic loads, namely the MTS model with model constants $C_{MTS} = 0.03$ and $C_T = 10$ and the WALE model with model constant $C_w = 0.325$. Grid G2 was used for this study. Good agreement was obtained between the different subgrid models, as seen in Figure 4. The difference between the maximum lift coefficients was less than 0.4% of the two models (C_{Lmax}= 2.74 for MTS and C_{Lmax}=2.73 for WALE model). There were some minor differences in the lift prediction during

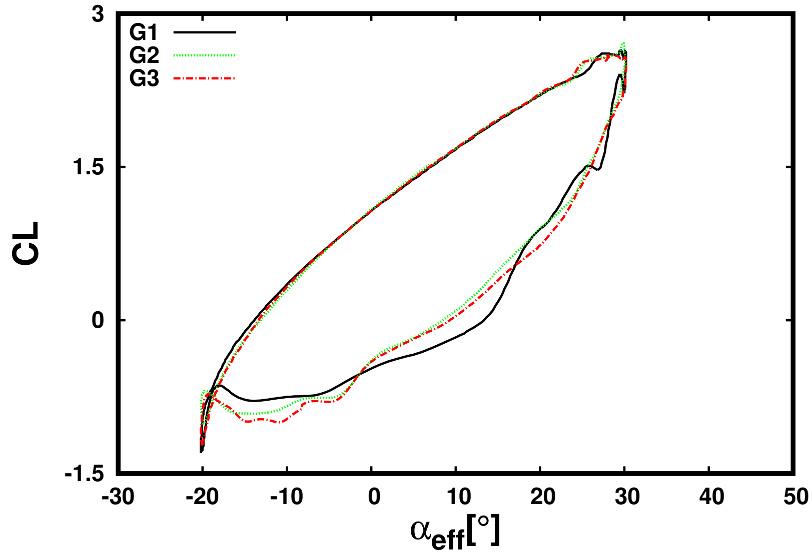

(a)

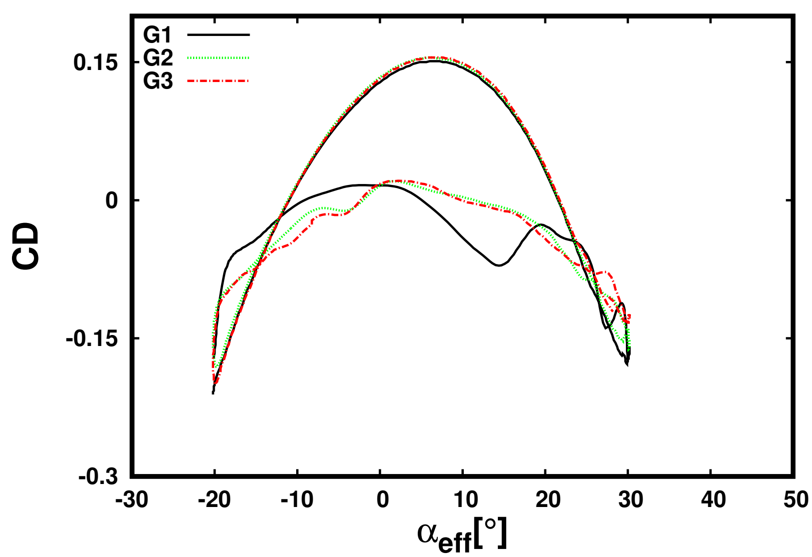

(b)

Figure 3: The effect of grid resolution on the computed aerodynamic loads: Lift (a), Drag (b), $\alpha = 5^{\circ}$, $Re_c = 2 \times 10^4$, $k = 0.94$ and $A/c = 0.5$.

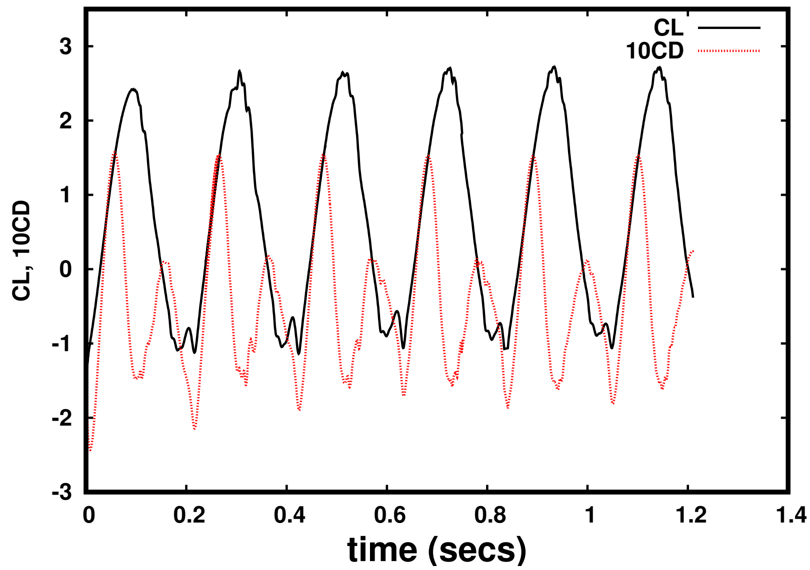

Figure 4: redTime series of lift and drag coefficient for grid G2, $\alpha = 5°$, $Re_c = 2 \times 10^4$, $k = 0.94$ and $A/c = 0.5$.

the wing's upwards displacement at $\alpha_{eff} = 30°$, where the WALE model produced a localised peak in the lift curve that was not seen for the MTS model.

3.3. Spanwise domain size

In the current computations the spanwise domain size was fixed to s=0.25c, similar to values adopted by [34] at comparable Reynolds numbers. In order to verify whether this size was sufficient, additional computations were conducted with a different spanwise size, i.e. s=1.0c. The corresponding grid was constructed using the G2 mesh, and the spacing in the spanwise direction, $\Delta z/c$, was kept fixed. Hence, the grid sizes were 645×249×43 and 645×249×172, representing s=0.25c and s=1.0c respectively. The effect of span width on the computed aerodynamic load is shown in Figure 6. The difference between the maximum lift coefficient was about 1.8% of the two domain widths and occurred at $\alpha_{eff} = 30°$. We have also looked into the flow fields (not shown here) and found that the key features of the flow (such as the LEV development) are not significantly changed. Similar tendencies has also been found by [22,36] who carried out investigations on the deep dynamic stall of a plunging wing at comparable Reynolds number

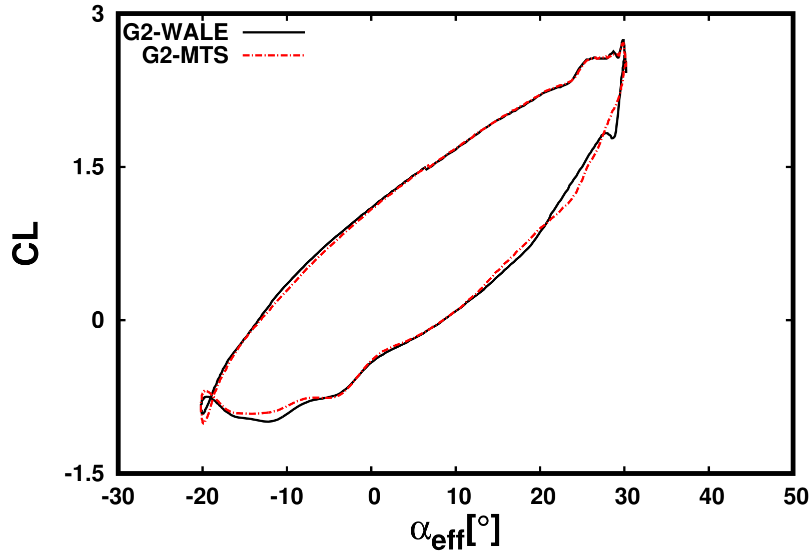

(a)

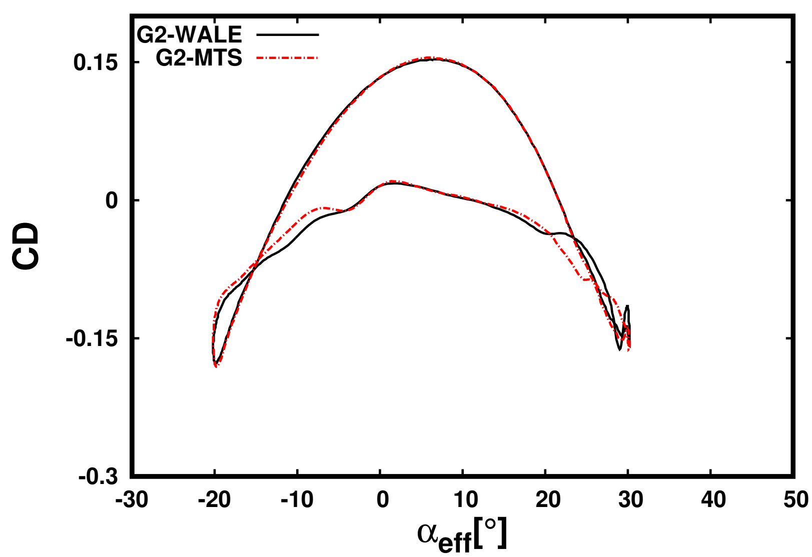

(b)

Figure 5: The effect of subgrid model on the computed aerodynamic loads: Lift (a), Drag (b), $\alpha = 5^{\circ}$, $Re_c = 2 \times 10^4$, $k = 0.94$ and $A/c = 0.5$.

to determine the relative importance of the spanwise width on the overall flow structure. We have also done a careful sensitivity study and found that the spanwise width does not show significant changes in the lift and drag coefficients (C_{Lave}=0.701 and C_{Dave}=-0.0416 for $s = 0.25c$ and C_{Lave}=0.689 and C_{Dave}=-0.0432 for $s = 1.0c$). Moreover the forces and flow field agree well with the experiments with $s = 5c$ for the two angle of attacks considered in the present study. Further extending the span width beyond $s = 1.0c$ is not expected to show any significant changes in the aerodynamic loads.

The results of all the different cases are in good agreement with each other, for example the maximum lift in all cases occurred at $\alpha_{eff} = 30°$ with less than 1.0% difference. For the main set of simulations grid G2, with span s=0.25c and the MTS subgrid model, representing a reasonable compromise in accuracy and computational cost, was chosen. All computations were run on 240 CPUs using the UK national supercomputing services Archer and each simulation using grid G2 required approximately 8 wall clock hours for one cycle.

4. Results

4.1. Aerodynamic loads

A comparison between LES and experimental water tunnel results for the pre-stall and post-stall heaving cases is shown in Figure 7 and 8, illustrating the variations of the phase-averaged lift coefficient as a function of the effective angle of attack and the time-averaged lift as a function of the heaving reduced frequency respectively. A semi-empirical model, Beddoes-Leishman dynamic stall model (LB) [37] has also been added in Figure 8 for comparison purposes. The phased-averaged experimental data were obtained through averaging over 55 cycles. As it was not feasible in the present computation to average over such a large number of cycles, the computed phase-averaged data for all comparison purposes have been averaged over three cycles. The LES results shown in Figure 7 agree closely with experiment over the whole heaving cycle, in particular at the lower reduced frequency (k=0.47). As the reduced frequency increases to k=0.94 there is a slight deviation between LES and the water tunnel measurements, especially during the increasing-lift part of the cycle. Specifically, the maximum lift is under-predicted by 10% for the pre-stall angle of attack of $\alpha = 5°$, which is associated with the first LEV formation and its convection. This is also reflected in the time-averaged lift results in Figure 8. Note that the sensitivity studies conducted

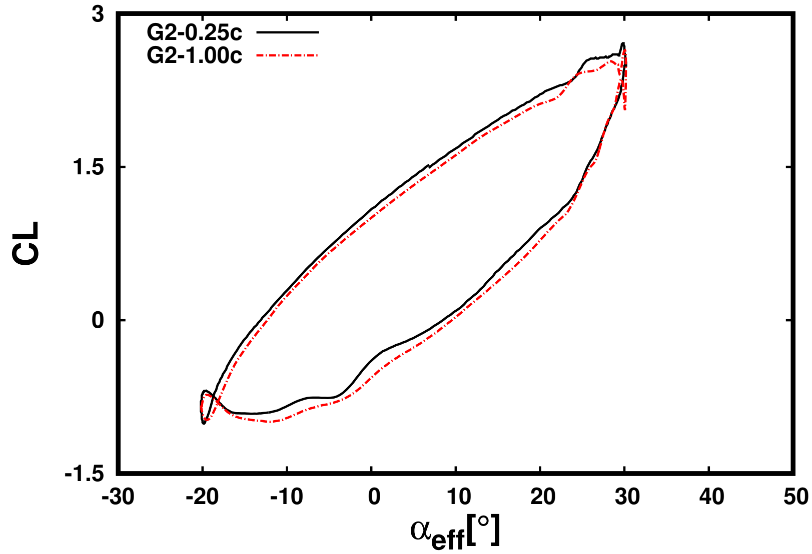

(a)

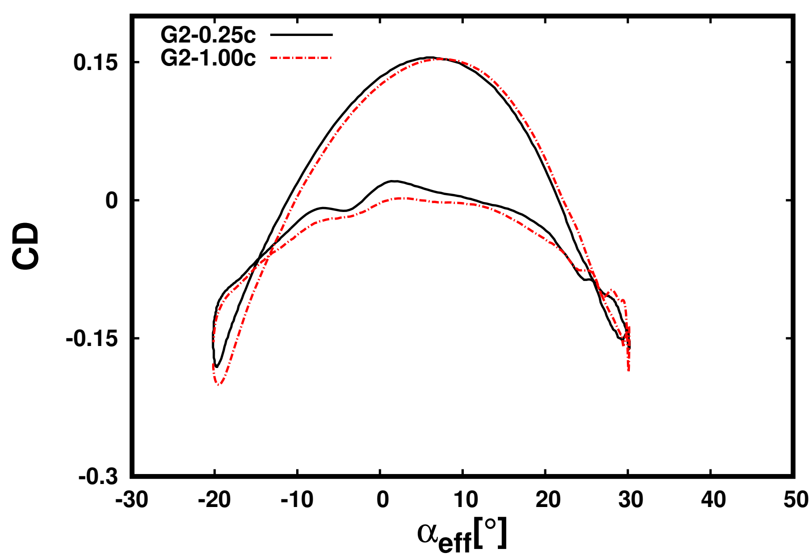

(b)

Figure 6: The effect of spanwise domain size on the computed aerodynamic loads: Lift (a), Drag (b), $\alpha = 5°$, $Re_c = 2 \times 10^4$, $k = 0.94$ and $A/c = 0.5$.

in Figures 3-6 did not show any significant differences in the hysteresis loop, hence the discrepancies cannot be attributed to the mesh, subgrid model or span width. Results from successive cycles did not also show any big differences, so extending the computations to include averaging over 55 cycles, as in the experiments, is not expected to provide significant improvement in the mean lift values. Potential causes for the discrepancies include support interference and inflow disturbance effects in the water tunnel where the experiments were performed with a turbulence intensity of less than 0.5%, none of which were included in the computations. End-wall effects also play a defining role in oscillating wing aerodynamic load predictions as has been addressed by [5, 38], who showed that the presence of a side wall can induce significant spanwise variations in the leading and trailing edge vortices during the dynamic stall process, thus influencing the aerodynamic loads. In the experiments the wing had end plates at the tip and root, however there was a gap of 2mm between the tip and the end plate, which accounts for about 3% of the chord. As the vortices become more three-dimensional, the gap could influence the tip flow and hence the tip vortex and the overall aerodynamic load prediction.

At pre-stall angles of attack the time-averaged lift (see Figure 7) exceeds the static value when the reduced frequency $k < 0.6$, with an increase of approximately 5% at k=0.94. For this angle of attack, the Beddoes-Leishman dynamic stall model shows a similar trend to both the experimental and computational results at low reduced frequency $k < 0.5$.

As the angle of attack is increased to post-stall conditions, the dependency of the time-averaged lift on the reduced frequency is more evident. There is a gradual increase in the time-averaged lift at $k < 0.5$ followed by a sudden increase of the slope for $k > 0.5$. Compared to the pre-stall angle of attack, at k=0.94 the time-averaged lift reaches values of about 120% higher than the static value. The trend in lift for the Beddoes-Leishman dynamic stall model deviates from both the computations and the measurements considerably, even at low reduced frequency.

4.2. Mean flow features

A view of the mean flow features is provided in Figures 9 and 10 for the pre-stall and post-stall condition respectively, showing the phase-averaged spanwise vorticity at three phases in the heaving cycle. At $\phi = 0°$, the wing is at its maximum displacement. An attached flow is observed in all cases and is more defined in terms of small-scale structures in the computations compared to the experiment. On the pressure side of the wing, some localised vortices can be seen at about $0.3c$. The LES also capture the trailing-edge separation and the near-wake vortical structures that were shed from the previous cycle. Similar tendencies can be observed for the post-stall angle of attack of $\alpha = 15°$ in Figure 10.

As the wing continues to move downwards from $\phi = 0°$ to $\phi = 90°$, it experiences an increase in effective angle of attack. Lift and moments change rapidly and the wing starts to undergo dynamic stall, which is characterised by the formation of the LEV. The computed and experimental flow structures are in close agreement. A reversed-flow region can be observed beneath the LEV. The trail of shed vortices from the previous cycle seen in the wake is also in qualitative agreement with the experiment. At the post-stall angle of attack the LEV increases in intensity and produces an increase in lift. The vortex appears to be much stronger in the LES and induces a region of negative vorticity over the suction side of the wing compared to the experiment.

As the wing continues to decelerate at $\phi = 180°$, it reaches its minimum point during the heaving motion. The main LEV has been shed downstream at about $0.5c$ and the trailing edge vortex (TEV) starts to emerge. The separation region with reversed flow between the main vortex and the secondary one at the leading edge is more prominent compared to $\phi = 90°$. The location and size of the LEV is in better agreement with the experiment for the post-stall condition.

At $\phi = 270°$, the LEV is now shed into the wake in both cases, however the size and location of the LEV differs between the computation and the experiment. Similar tendencies can be observed for the post-stall angle of attack of $\alpha = 15°$ in Figure 10.

4.3. Instantaneous flow features

4.3.1. Pre-stall, $\alpha = 5°$

As the effective angle of attack increases, the LEV is initiated. As the LEV rolls up and convects downstream an increase in lift occurs, since the LEV enlarges the effective camber of the wing. The process of transition of the LEV is a significant feature of the dynamic stall process, as it influences the aerodynamic loads. The characteristics of the LEV system and its transition to turbulence are therefore investigated for $\alpha = 5°$, $k = 0.94$ (Figures 11-15). Figure 11 shows signals taken using 100 probes placed one cell above the suction surface of the wing, evenly distributed in x at the same spanwise location. The signals corresponds to the fluctuating vertical velocity, v', and

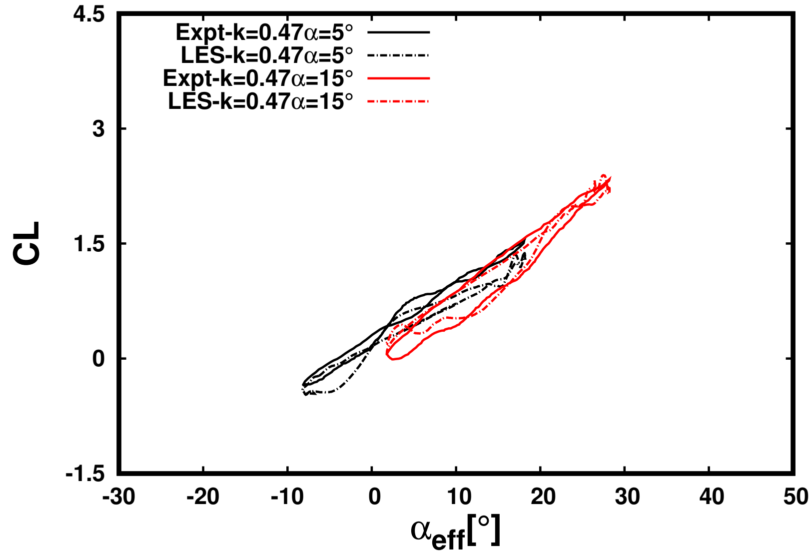

(a) k= 0.47

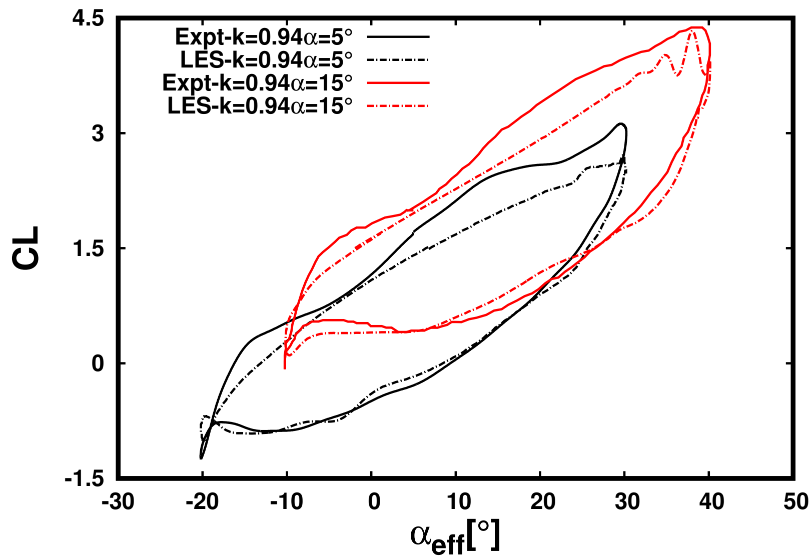

(b) k= 0.94

Figure 7: Phase-averaged lift coefficient as a function of the heave-induced effective angle of attack, $A/c = 0.5$; $\alpha = 5^{\circ}$ and 15°, $Re_c = 2 \times 10^4$; Experimental results from [35].

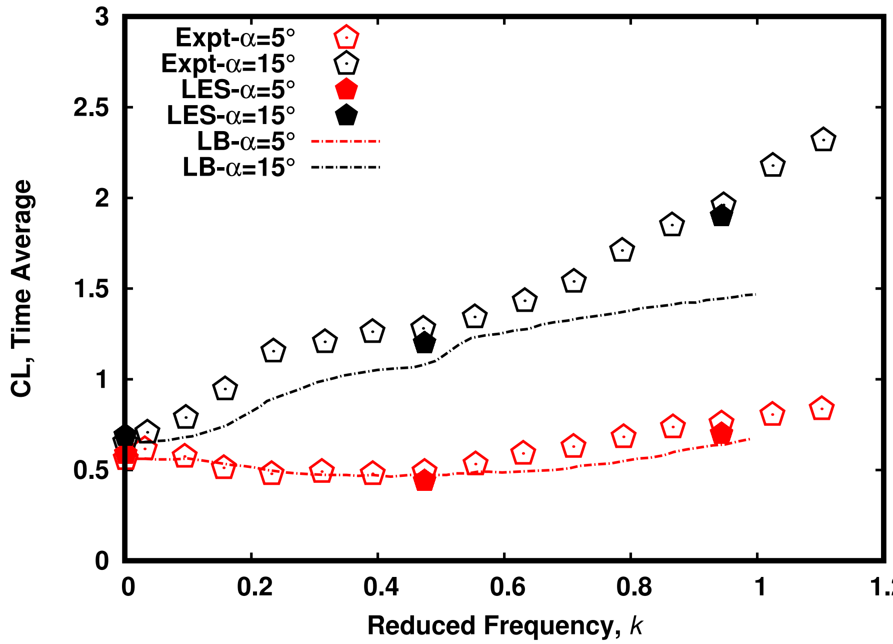

Figure 8: Time-averaged lift as a function of the heaving reduced frequency for k, $A/c = 0.5$; $\alpha = 5°$ and $15°$, $Re_c = 2 \times 10^4$; LB denotes Leishman-Beddoes model. Experimental results from [35].

were staggered by their chordwise (x/c) position relative to the leading edge. The v' signals were taken for one cycle of the heaving motion. High fluctuations are distinguished as regions of high vorticity and may be characterised by flow separation, re-attachment and transition to turbulence. A closer inspection of Figure 11 and the vorticity fields (for 3 cycles) shows that the flow is three-dimensional, unsteady, vortical and more random. Therefore it is identified as incipient turbulence from the leading edge (at x/c=0.04) up to the mid-chord (at x/c=0.5) between ϕ =65° $-$ 180° (hereafter termed region A). The flow re-laminarises as it approaches the trailing edge (from x/c = 0.5-1.0). This is also confirmed in the power spectral density plot of the fluctuating vertical velocity signals at various x/c in Figure 12 where the peak and overall levels are reduced for $x/c = 1$ when compared with the other locations in region A. Portions of the spectrum around frequency 10-100Hz is not inconsistent with the emergence of a small inertia sub-range. The turbulent structures in region A occur during the wing's downwards displacement until the wing reaches its minimum point. Figure 14(c-l) shows ten snapshots (in

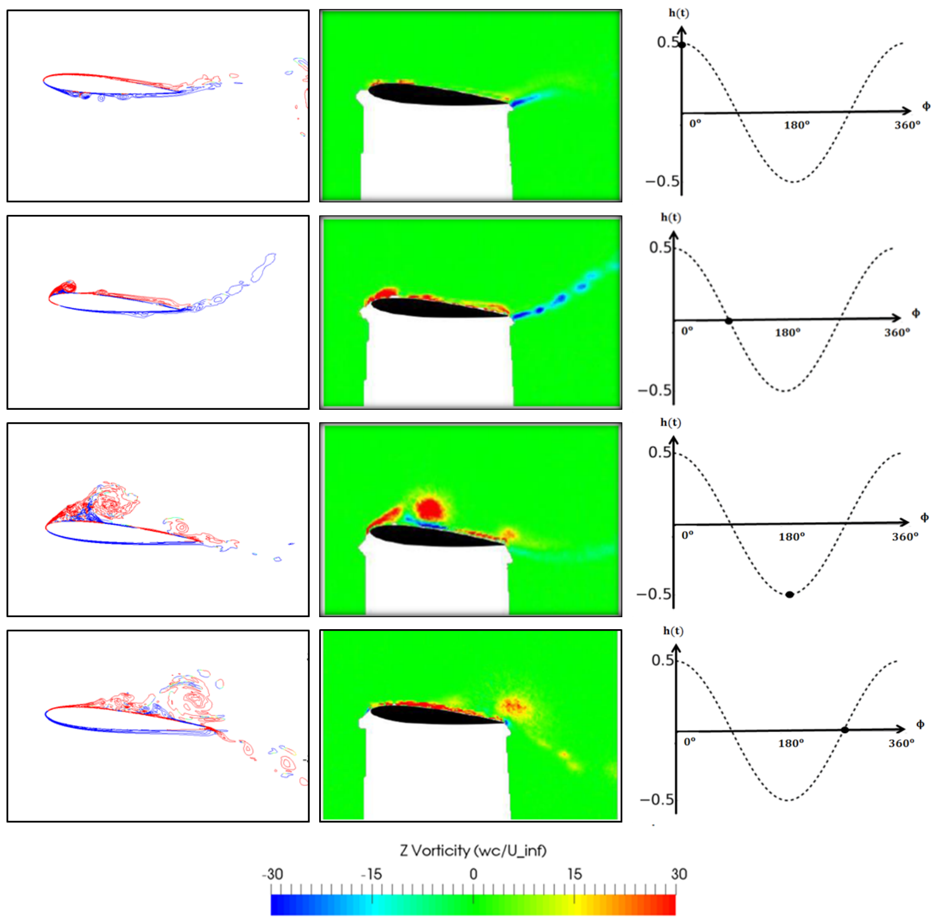

Figure 9: Phased-averaged contour plot of spanwise vorticity, w_z for $Re_c = 2\times10^4$, $\alpha = 5^0$, $k = 0.94$ and $A/c = 0.5$: LES(left); Expt(middle)[35]; Displacement (right).

region A) of isosurfaces of instantaneous vorticity magnitude showing three-dimensional flow structures on the suction side of the heaving wing. Figures 14a and b have also been included to emphasise that the boundary layer of the wing was laminar up until ϕ=65°, when the emergence of the first LEV denoted L1 was observed. L1 is initially two-dimensional in nature with no spanwise variations. The flow is mostly attached, with some separation at the trailing edge, as seen in the skin friction plot in Figure 13. L1 then grows in size from ϕ=65° − 86°, still retaining its coherent structure. At ϕ=86° (see also Figure 16) three clockwise vortices can be observed, namely L1 (now at $x/c = 0.11$), a secondary vortex (L2) upstream of L1 at $x/c = 0.057$, and a

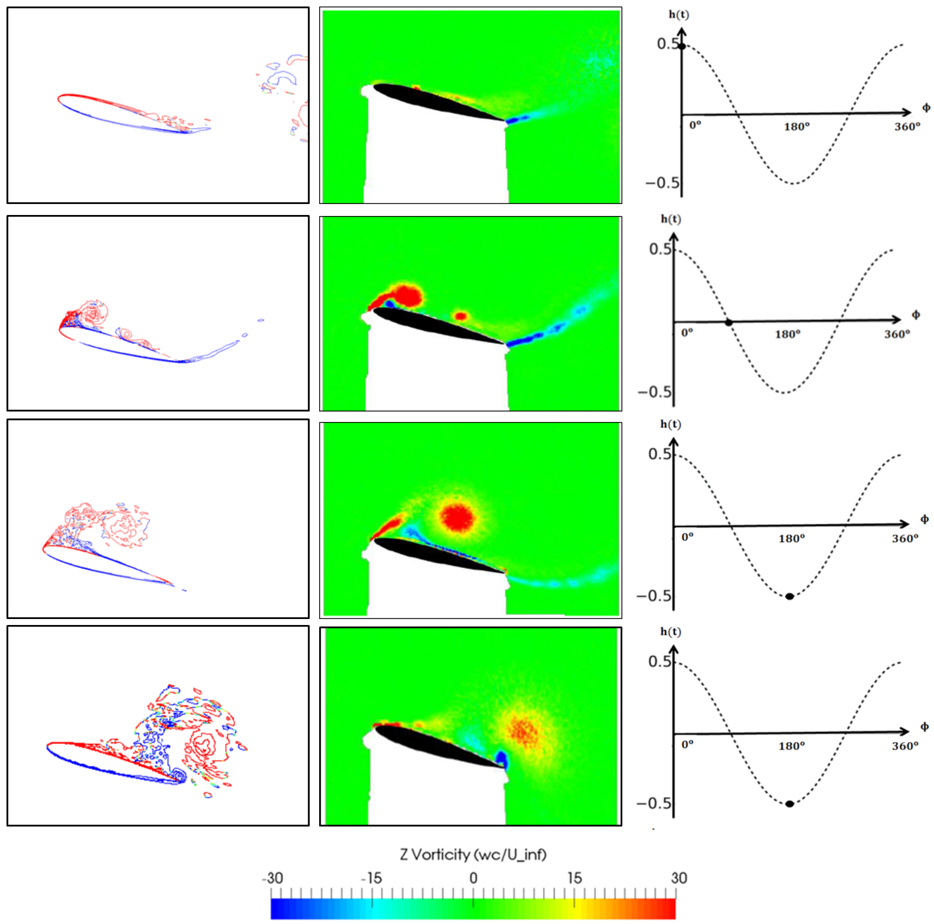

Figure 10: Phased-averaged contour plot of spanwise vorticity, w_z for $Re_c = 2 \times 10^4$, $\alpha = 15^0$, $k = 0.94$ and $A/c = 0.5$: LES(left); Expt(middle)[35]; Displacement (right).

third vortex structure (L3) at $x/c = 0.3$. Spanwise instabilities at the leading edge start to appear at ϕ=93°, which is seen more clearly in the surface plot in Figure 15g. The corresponding skin friction plot in Figure 13 (ϕ=93°) shows evidence of separation at the leading edge. L1 starts to breakdown from ϕ=101° − 108°. By ϕ=144°, spanwise instability is more visible. Skin friction plots show that the unsteady boundary layer separates at around x/c = 0.2. A single vortex structure containing small scale turbulent structures characterises the flow features in this region. The shedding of L1 continues from ϕ=158°, reaching about x/c = 0.5 at ϕ=180°, which is the minimum point of the heaving motion.

4.3.2. Instability mechanism, $\alpha = 5°$

The preceding section identified instabilities around the core of the LEV system. From the three-dimensional plots in Figure 14, it is difficult to observe the core of the vortices since they are masked by w_z (spanwise) vortical structures wrapped around the vortices. Instead, in order to understand the instability and their underlying mechanisms, contours of w_z plotted for $(x - z)$ planes through the various vortex structures are evaluated. The plots are carried out at $\phi = 86°$ as shown in Figure 16(left), where point A is a clockwise vortex previously denoted as $(L2)$, B is the saddle point region, C (previously denoted $L1$) and is also a clockwise vortex. D and E are the recirculating regions respectively where the vortices are anti-clockwise in nature. Figure 17(right) shows the location of $(x - z)$ planes through all the structures $A - E$.

In Figure 16(left), B is two-dimensional in nature and the perturbations inside the core of C are of non-uniform amplitude across the span, much larger over the range 0.004 < z < 0.007 (see also Figure 18). A is also three-dimensional in nature (Figure 16 middle). It is interesting to note that the amplitude is larger than that of C as seen in Figure 18. The core of the recirculation regions, D (Figure 16 right) and E (Figure 16 middle) indicated by the blue colours in both plots also exhibit variations but with much lower amplitude across the span compared to A and C.

The origin of the spanwise variations can be explained by referring back to the plots in Figure 14. As the wing begins its downstroke manoeuvre, a small region of reverse flow (D) develops on the wings suction surface. D grows in size from ϕ=50° to ϕ=86°, moving upstream toward the leading edge and giving rise to instabilities in the detached shear layer which is starting to roll up. The shear layer rolls above a laminar separation bubble, consisting of several vortices, A, C and E. Notice that D is in phase with A and suggests that the original three-dimensionality of A may be a result of large scale deformation of the vortex caused by the contact with the reverse vortex rather than originating from the growing disturbances within A. The "transition by contact", due to flow reversal observed by [39] is similar to the mechanism seen here.

Within the core of C, w_z seems to have broken down into small scale structures with wavelength of a similar order of magnitude to that associated with elliptic instability. Elliptic instability is associated with vortex stretching and the instability is usually a spanwise deformation of the vortex core. Leweke and Williamson [40] suggested values of the order of $\lambda = 3\text{D-}4\text{D}$ (where λ is the spanwise wavelength and D is the diameter of the region of elliptical flow) for the most amplified instability mode. This is also supported by [41-43]. From Figure 19, it can also be observed that the development of the core of the vortices appear to contain varicose as well as sinuous features. Thus a potential mechanism for the breakdown is the presence of elliptic instability of the vortex cores (A and C), initiated by contact with the reverse flow vortex D. Since D is caused by C, the whole process forms a feedback loop.

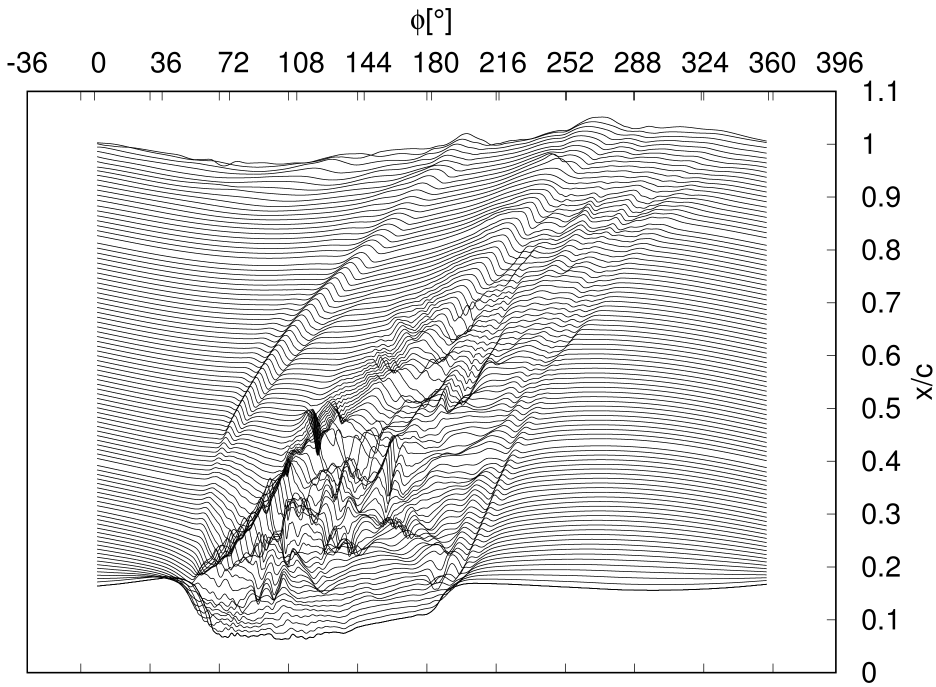

Figure 11: Instantaneous vertical velocity signals v'; $Re_c = 2 \times 10^4$, $\alpha = 5°$, $k = 0.94$ and $A/c = 0.5$. The maximum and minimum amplitude of v' is 0.317m/s and -0.223m/s respectively.

4.3.3. Post-stall, $\alpha = 15°$

At the post-stall angle of attack, the effect of the LEV is stronger as shown in Figure 20 (a-l). At ϕ =50° the LEV, L1 has already been initiated. L1 was first observed at ϕ =30° (not shown here). L1 continues to grow in

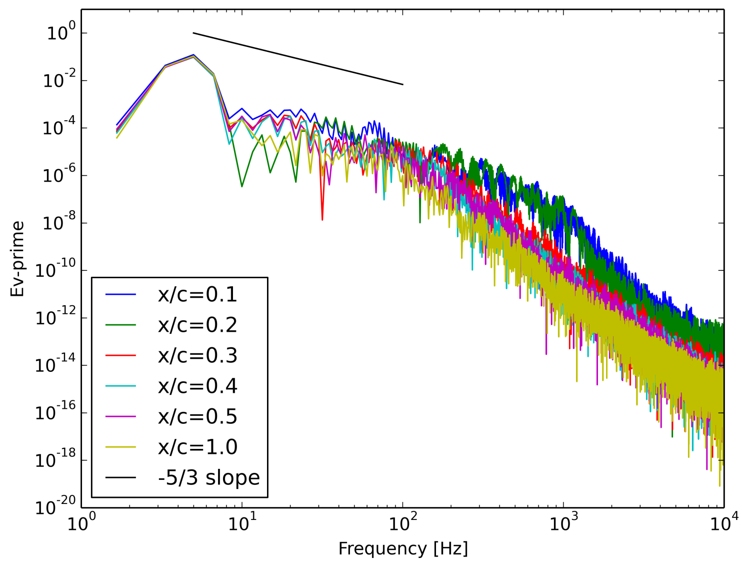

Figure 12: Power spectral density of instantaneous vertical velocity values one cell above the suction surface of the wing at $x/c = 0.1, 0.2, 0.3, 0.4, 0.5$ and 1.0, sampled at mid-span. $Re_c = 2 \times 10^4$, $\alpha = 5°$, $k = 0.94$ and $A/c = 0.5$.

size from ϕ=57° − 72° where spanwise instabilities at the leading edge first start to appear outside the vortex core. Similar to the pre-stall angle of attack, at ϕ=86° structures L1, L2 and L3 can also be observed outside the vortex core. However, within the core of the vortex, there are differences in shape, size and positions of vortices A-E compared to the pre-stall angle of attack (in Figure 16), as seen from the plot in Figure 21. The shedding of L1 continues until ϕ=180°.

Note that as a result of the increase in strength and size of the LEV from $\alpha = 5°$ to $\alpha = 15°$, the time-averaged lift of the latter increases compared to the static value at $\alpha = 15°$. The effect on the amplitude seems to be minimal. At high frequency the cyclic variation is dominant due to the added mass force. This makes most theoretical models such as the Theodorsen model still able to predict the amplitude of the lift periodical oscillations even at $k \approx 0.94$, where strong coherent vortical structures invalidate the theory behind the model (irrotational flow hypothesis). On the other hand, the LEV produces an increase in time-averaged lift with respect to the static value that the Theodorsen theory cannot predict.

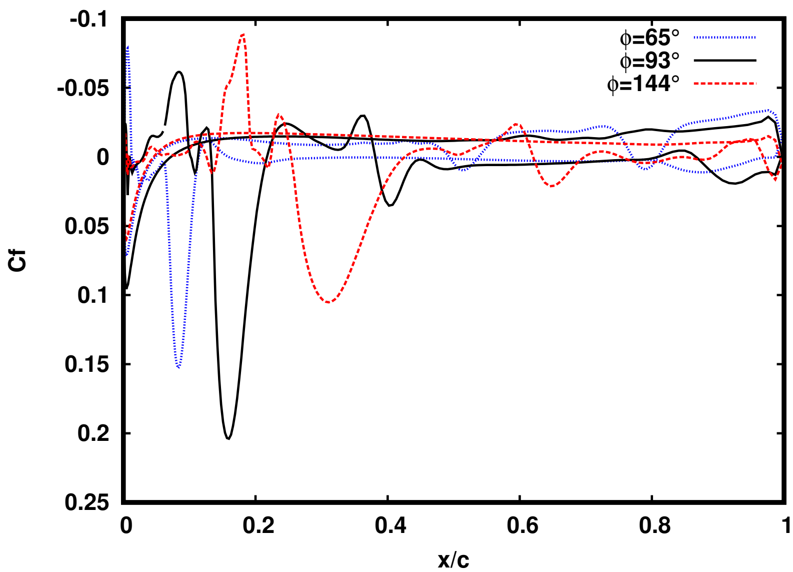

Figure 13: Skin friction coefficients at $\phi = 65^\circ - 144^\circ$, $Re_c = 2 \times 10^4$, $\alpha = 5^\circ$, $k = 0.94$ and $A/c = 0.5$.

5. Reynolds number influence

5.1. Pre-stall, $\alpha = 5^\circ$

The influence of Reynolds number on the LEV system and its transition to turbulence on the heaving wing was investigated for $Re_c = 2 \times 10^4$ and 5×10^4. Two separate grids G1 and G2 ($y1^+$ values similar to Table 2) were employed and compared for the higher Reynolds number. The corresponding aerodynamic forces are shown in Figure 22. The lift plots agree closely with each other over the whole heaving cycle. The maximum lift is also comparable, however there is a slight downwards shift in drag coefficient when the Reynolds number is increased, which could be associated with the difference of vortex shedding at large effective angle of attack. The maximum discrepancy of C_D between $Re_c = 2 \times 10^4$ and $Re_c = 5 \times 10^4$ is approximately 10% of the maximum variation of C_D during one cycle. Interestingly, the drag coefficient at $Re_c = 5 \times 10^4$ is less sensitive to the resolution than at Re_c $= 2 \times 10^4$ and we do not expect any significant difference in flow features between the two resolutions for $Re_c = 5 \times 10^4$. The Reynolds number effect on the instantaneous flow features is shown in Figures 23 to 25 for Re_c $= 5 \times 10^4 - G1$. Unlike the $Re_c = 2 \times 10^4$ case, which showed turbulent

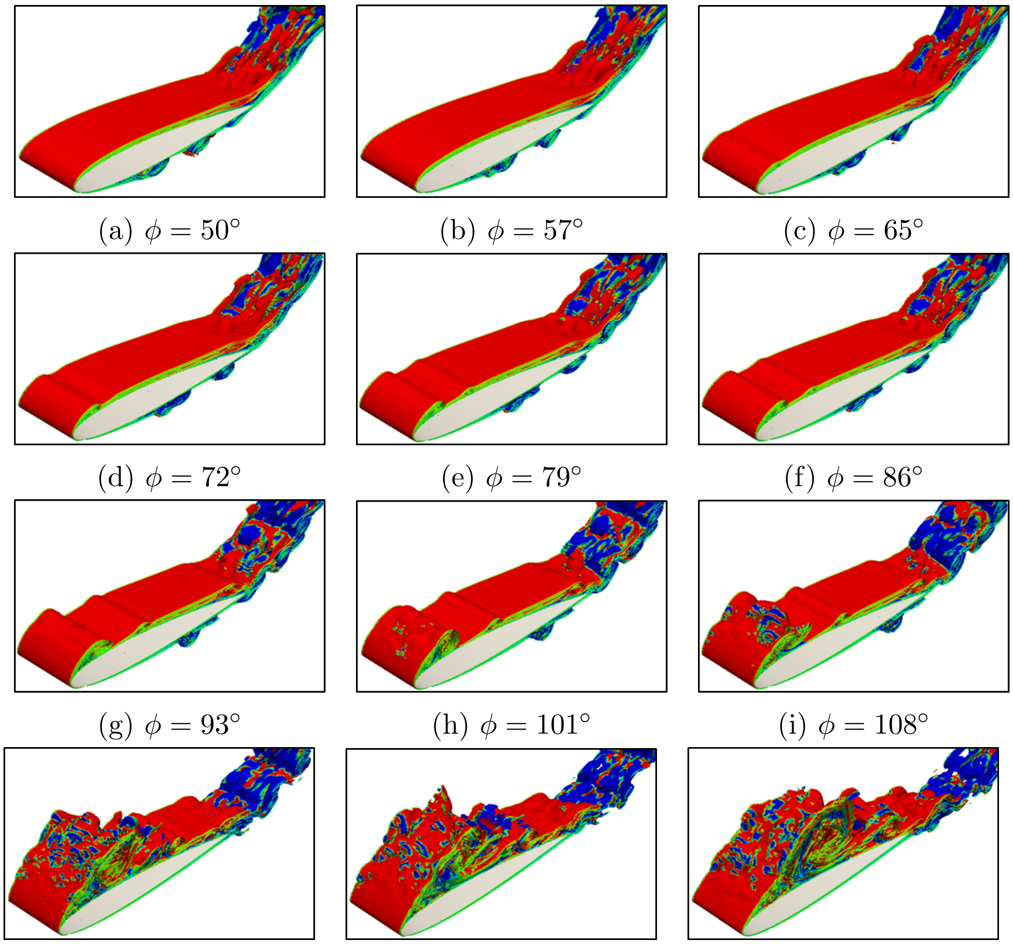

(a) $\phi = 50^\circ$ (b) $\phi = 57^\circ$ (c) $\phi = 65^\circ$

(d) $\phi = 72^\circ$ (e) $\phi = 79^\circ$ (f) $\phi = 86^\circ$

(g) $\phi = 93^\circ$ (h) $\phi = 101^\circ$ (i) $\phi = 108^\circ$

(j) $\phi = 144^\circ$ (k) $\phi = 158^\circ$ (l) $\phi = 180^\circ$

Figure 14: Isosurfaces of instantaneous vorticity, w_z over the range of ± 30 for $Re_c = 2 \times 10^4$, $\alpha = 5^\circ$, $k = 0.94$ and $A/c = 0.5$.

structures at the leading edge up until mid chord followed by relaminarisation towards the trailing edge (see Figure 11), for $Re_c = 5 \times 10^4$, turbulent structures can be observed all the way to the trailing edge (see Figure 23). The trailing edge vortex TEV has a higher strength compared to the lower Reynolds number case. At $Re_c = 5 \times 10^4$, L1 is first observed at $\phi = 57^\circ$ and spanwise instabilities starts to occur at $\phi = 72^\circ$ (see Figures 23 and 24). Instability effects become apparent at the bottom of the downstroke for both Re_c but much earlier at $\phi = 101^\circ$ for $Re_c = 5 \times 10^4$. At $\phi = 270^\circ$ in Figure

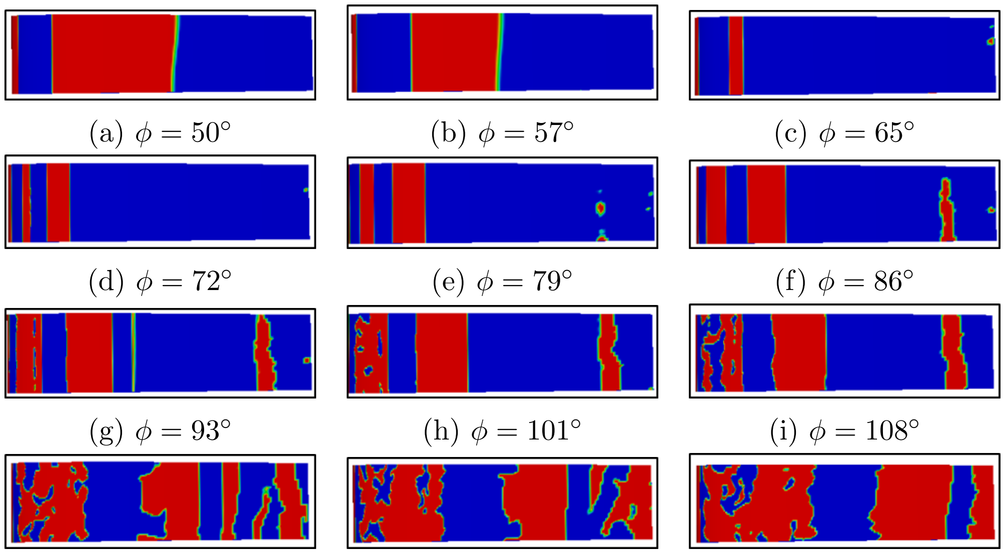

(a) $\phi = 50°$ (b) $\phi = 57°$ (c) $\phi = 65°$

(d) $\phi = 72°$ (e) $\phi = 79°$ (f) $\phi = 86°$

(g) $\phi = 93°$ (h) $\phi = 101°$ (i) $\phi = 108°$

(j) $\phi = 144°$ (k) $\phi = 158°$ (l) $\phi = 180°$

Figure 15: Instantaneous spanwise vorticity, w_z over the range of ± 30, near the wing suction surface during transition for $Re_c = 2 \times 10^4$, $\alpha = 5°$, $k = 0.94$ and $A/c = 0.5$.

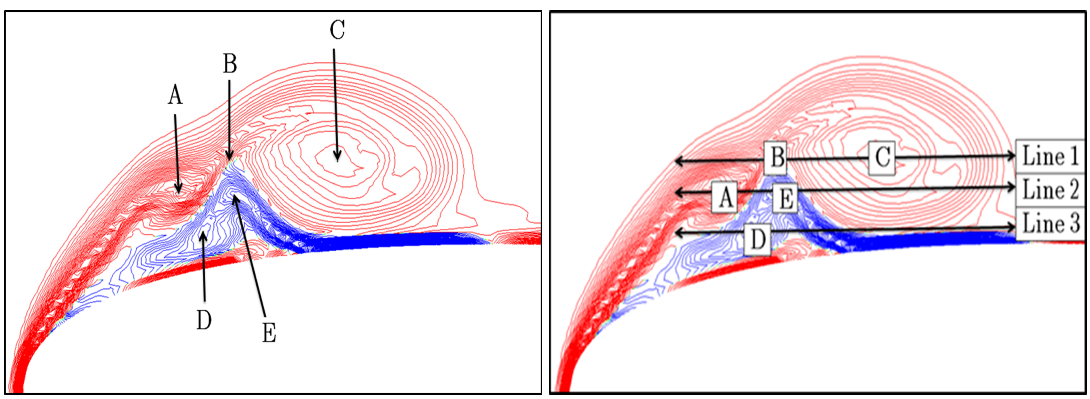

Figure 16: Left: Contours of w_z over the range of ± 30 taken across the centres of vortex cores with (x,y)co-ordinates A(0.057c, 0.142c), B(0.072c, 0.149c), C(0.113c, 0.160c), D(0.065c, 0.136c) and E (0.072c, 0.140c); Right:(x-z) planes through the cores of B&C (Line1), A&E (Line2) and D (Line 3) at $\phi = 86°$, $Re_c = 2 \times 10^4$, $\alpha = 5°$, $k = 0.94$ and $A/c = 0.5$.

24, the TEV and near wake structures are turbulent for the higher Reynolds number. The TEV was found to interact with L1. The complex vortical structures may explain the slight shift in the C_D plot and also the decrease

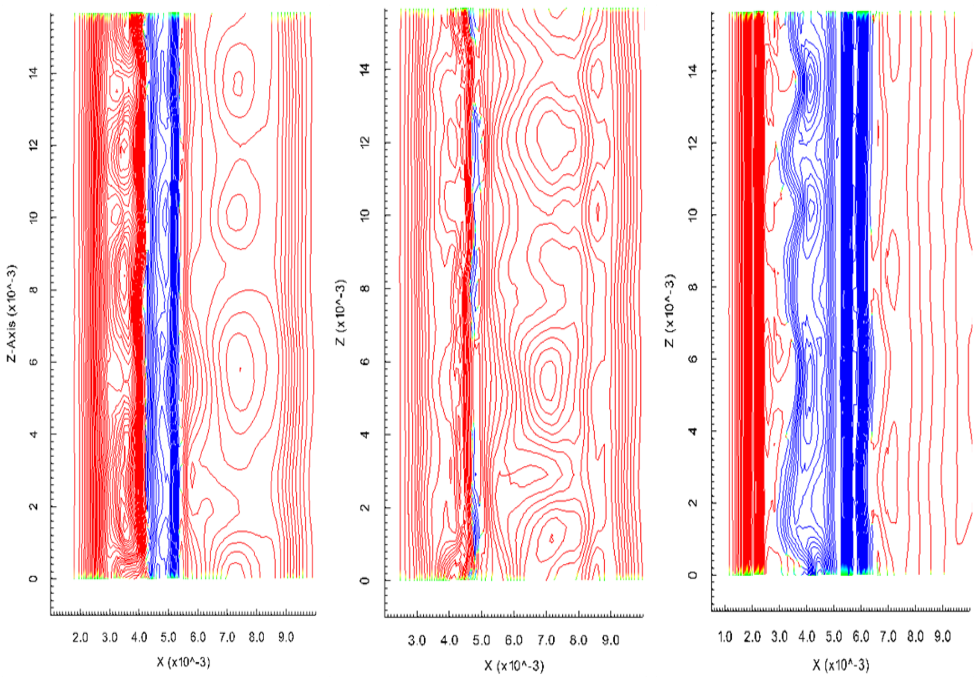

Figure 17: Contours of w_z over the range of ± 30, showing the x-z cut plane passing approximately through vortex cores, Left(Line 1); Middle(Line 2); Right(Line 3) at $\phi = 86°$, $Re_c = 2 \times 10^4$, $\alpha = 5°$, $k = 0.94$ and $A/c = 0.5$.

in $C_{D_{max}}$ at the high Reynolds number.

This finding is very important as it shows that Re_c influences not only the flow structures but also the aerodynamic loads. This is also supported by the findings of [44] who also investigated the influence of both Strouhal and Reynolds number on a plunging wing at low Reynolds number.

6. Conclusions

An advanced LES approach, to gain insight into the characteristic phenomena of the dynamic stall process, and more especially the LEV formation and transition, has been presented. The results of the sensitivity analysis of grid, domain extent and subgrid model were in good agreement with each other. The maximum lift in all cases occurred at $\alpha_{eff} = 30°$ with less than 1.0% difference.

The aerodynamic hysteresis also showed good agreement with experimental water tunnel measurements over the whole heaving cycle at reduced

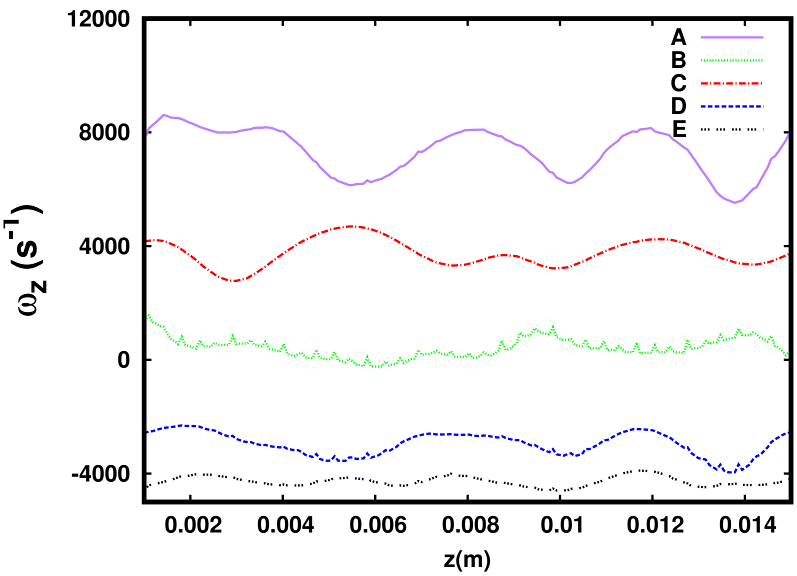

Figure 18: Contours of w_z passing approximately through vortex A to E centres at $\phi = 86°$, $Re_c = 2 \times 10^4$, $\alpha = 5°$, $k = 0.94$ and $A/c = 0.5$.

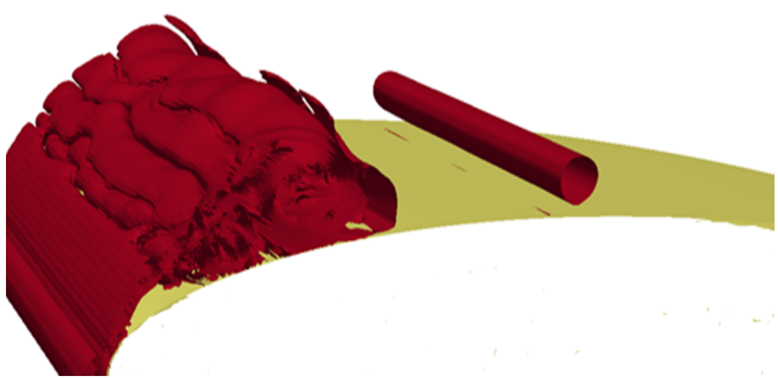

Figure 19: Instantaneous flow configuration (on the wing suction surface) for the varicose breakdown of the spanwise streak within the core of vortex C, displayed in terms of Q-criterion isosurface (Q=500) at $\phi = 86°$, $Re_c = 2 \times 10^4$, $\alpha = 5°$, $k = 0.94$ and $A/c = 0.5$.

frequencies, $k = 0.47$ and $k = 0.94$, with better agreement at the lower reduced frequency.

Analysis of the mean flow features revealed that when the angle of attack increases from pre-stall to post-stall, the size of the LEV increases and there

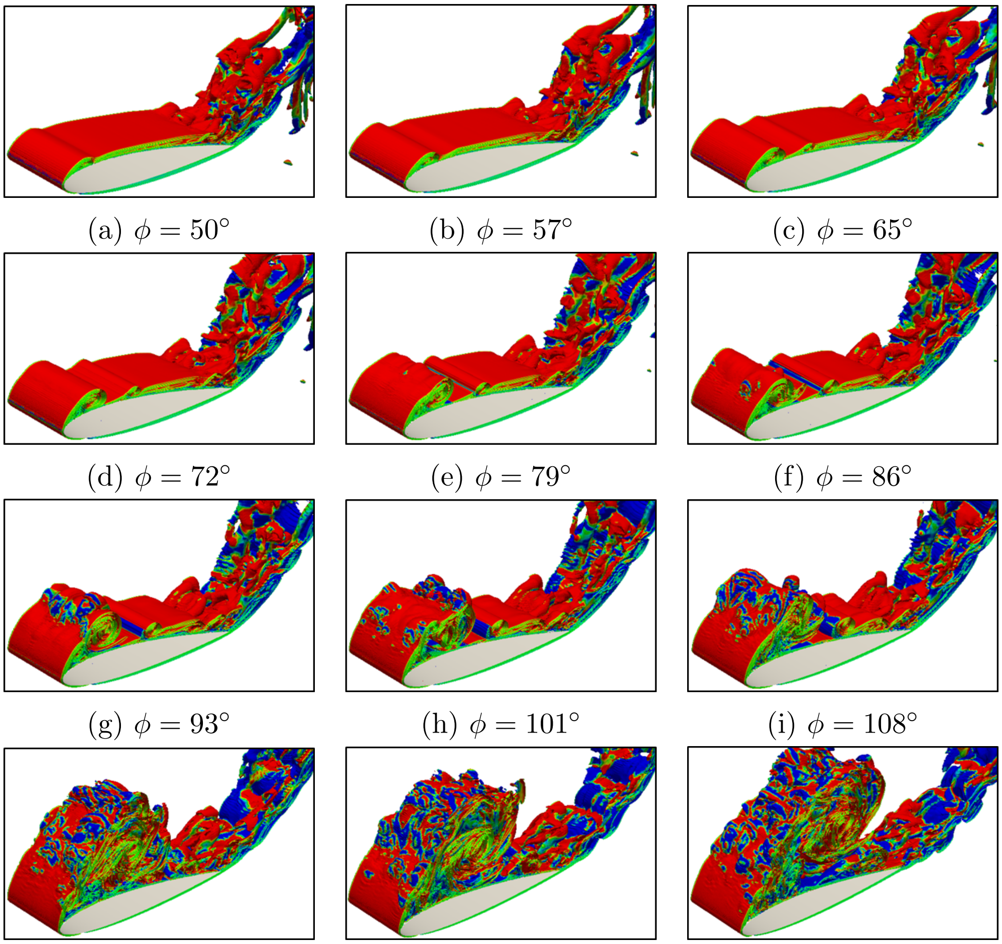

(a) $\phi = 50°$ (b) $\phi = 57°$ (c) $\phi = 65°$

(d) $\phi = 72°$ (e) $\phi = 79°$ (f) $\phi = 86°$

(g) $\phi = 93°$ (h) $\phi = 101°$ (i) $\phi = 108°$

(j) $\phi = 144°$ (k) $\phi = 158°$ (l) $\phi = 180°$

Figure 20: Isosurfaces of instantaneous vorticity w_z over the range of ± 30, for $Re_c = 2 \times 10^4$, $\alpha = 15°$; $k = 0.94$ and $A/c = 0.5$.

is a delay in the laminar to turbulent transition process. The increase in size of the LEV also increases the time-averaged lift compared to static lift at post-stall angle of attack, however its effect on the amplitude appears to be minimal.

Detailed analysis of the instantaneous flow structures at pre-stall angle of attack was also provided, with emphasis on the role of the instability mechanism in the separation bubble transition on the wing suction surface. Starting from a laminar boundary layer, as the wing was on its downstroke

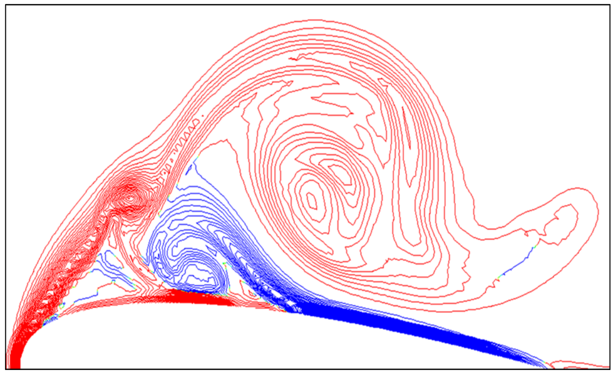

Figure 21: Contours of w_z at $\phi = 86°$ over the range of ± 30, $Re_c = 2 \times 10^4$, $\alpha = 15°$, $k = 0.94$ and $A/c = 0.5$.

manoeuvre, the first LEV was observed at around $\phi = 65°$. The LEV grew in size whilst retaining its coherent structure until $\phi = 85°$. The LEV system was found to be two-dimensional in nature outside its core. The vortex structure breaks down into smaller scale structures within the core, suggesting the presence of an elliptic instability. The reverse vortex was also found to be three-dimensional and also in phase with the secondary vortex L2 suggesting that the shear layer starting to roll up might already be three-dimensional in nature with the recirculation providing a feedback of the three-dimensional disturbances from the developing LEV. The three-dimensional unsteady (i.e. incipient turbulence) disturbances within the core of the reverse vortex were observed to be present down to the wing surface near the leading edge.

The influence of Reynolds number on the lift and drag coefficient was investigated for the pre-stall angle of attack and details of the flow patterns and vortical structures examined. The effect on lift coefficient is minimal but its influence on the drag coefficient is visible. The maximum drag coefficient decreases as Re_c increases. At $Re_c = 5 \times 10^4$, the TEV is more pronounced and there is a delay in the shedding of the TEV. This is consistent with the slightly lower drag coefficient.

This work has focused on the separation bubble at the leading edge on the suction surface of a heaving wing. Future work should focus on investigating the instabilities at the trailing edge during the heaving cycle in particular in combination with a pitching motion as well as external disturbance effect.

In the present contribution, the capability of large-eddy simulation has been successfully demonstrated for separated flows at low Reynolds number.

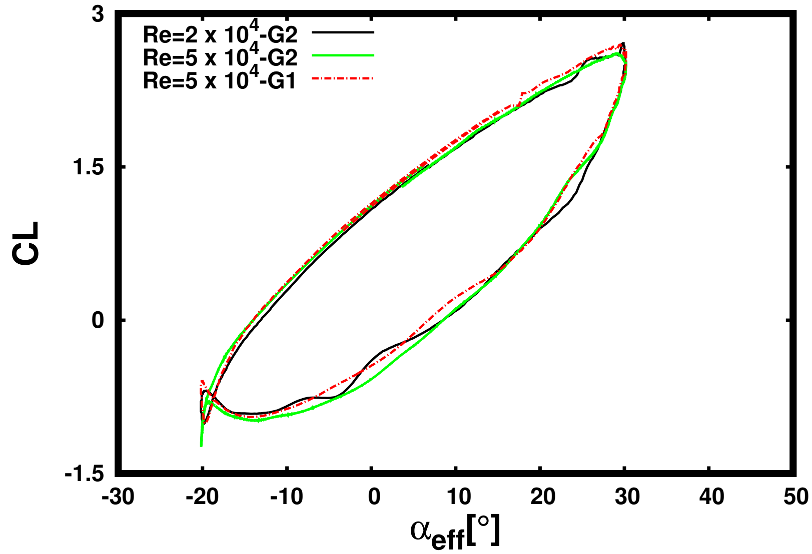

(a)

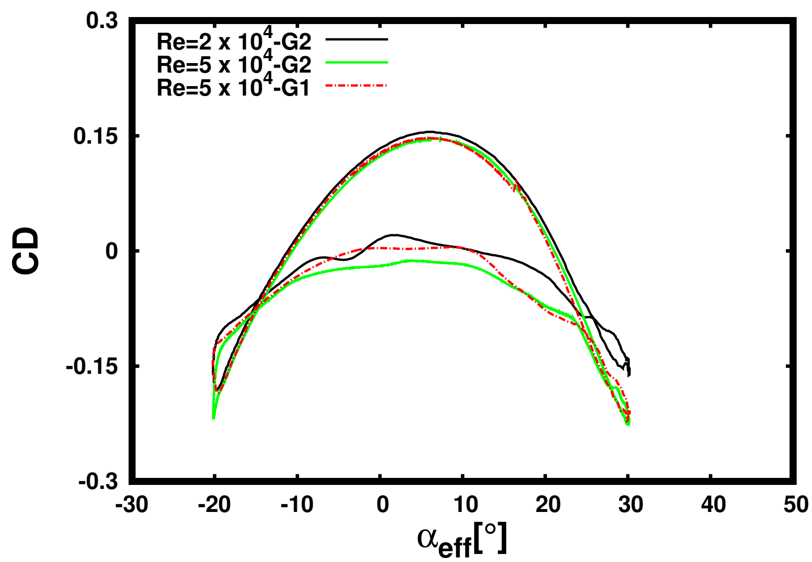

(b)

Figure 22: The effect of Reynolds number on the computed aerodynamic loads: Lift (a), Drag (b), $\alpha = 5°$, $k = 0.94$ and $A/c = 0.5$.

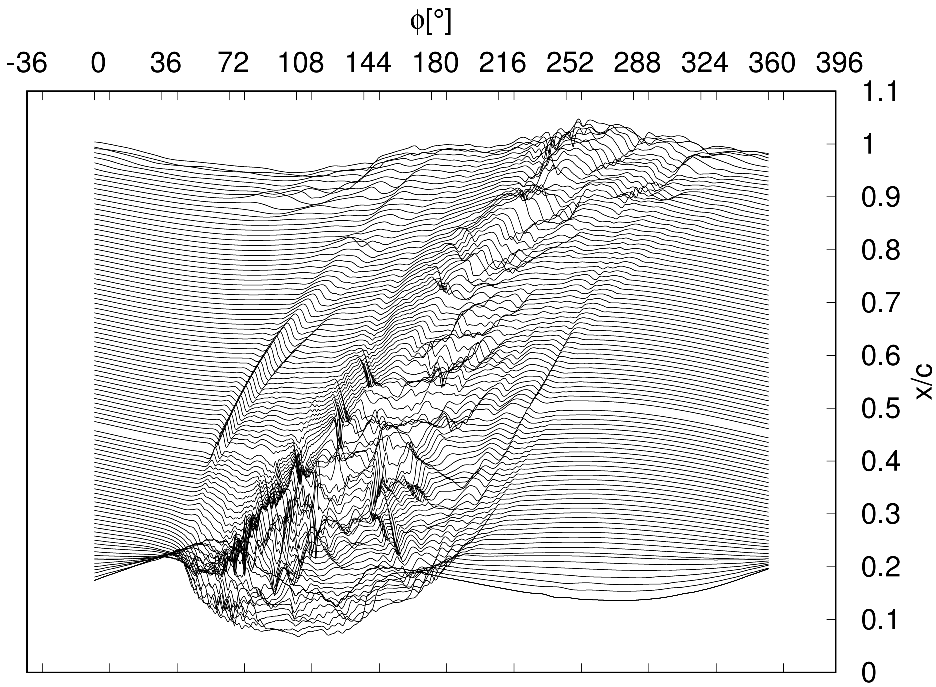

Figure 23: Instantaneous vertical velocity signals v'; $Re_c = 5 \times 10^4$, $\alpha = 5°$, $k = 0.94$ and $A/c = 0.5$. The maximum and minimum amplitude of v' is 0.381m/s and -0.320m/s respectively.

Acknowledgements

This work was supported by the Engineering and Physical Sciences Research Council (EPSRC) grant EP/M022692/1. The authors acknowledge the use of IRIDIS High Perfomance Computing Facility at the University of Southampton and the UK National Supercomputing Service Archer supported by the EPSRC under grant EP/L000261/1. The authors are also grateful to Kensley Balla for discussions during the early stages of this work. Lift and drag data are available from the University of Southampton data repository under DOI:10.5258/SOTON/D0524.

[1] Wang, Z.J. Two dimensional mechanism for insect hovering. *J. Phys Rev.* (2000) **85**:2216–2219.

[2] Lewin, G.C. and Haj-Hariri, H. Modelling thrust generation of a two-

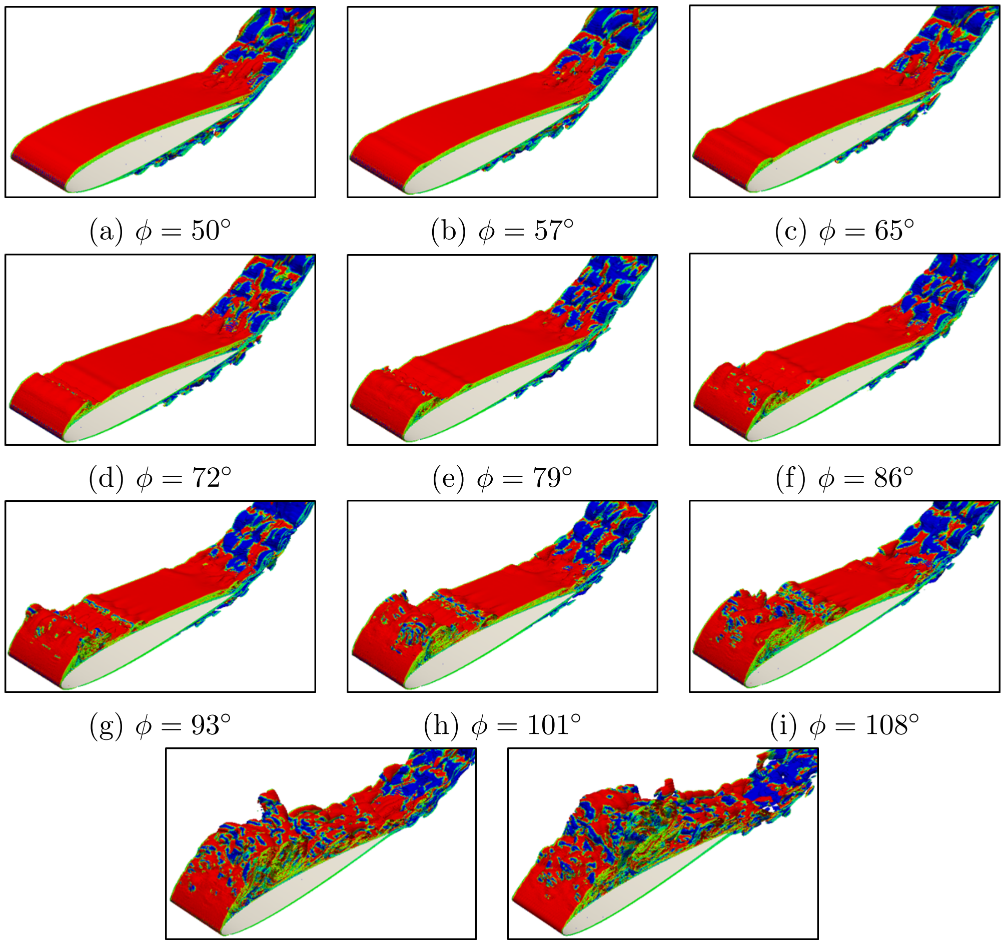

(a) $\phi = 50°$ (b) $\phi = 57°$ (c) $\phi = 65°$

(d) $\phi = 72°$ (e) $\phi = 79°$ (f) $\phi = 86°$

(g) $\phi = 93°$ (h) $\phi = 101°$ (i) $\phi = 108°$

(j) $\phi = 144°$ (k) $\phi = 180°$

Figure 24: Isosurfaces of instantaneous vorticity w_z over the range of ± 30, for $Re_c = 5 \times 10^4$, $\alpha = 5°$; $k = 0.94$ and $A/c = 0.5$.

dimensional heaving wing in a viscous flow. *J. Fluid Mech.* (2003) **492**:339–362.

[3] Sandham, N.D., Sandberg, R.D. and Jones, L.E. Direct numerical simulation of forced and unforced separation bubbles on a wing at incidence. *J. Fluid Mech.* (2008) **602**:175–207.

[4] Akbari, M.H. and Price, S.J. Simulation of dynamic stall for a NACA0012 airfoil using vortex method. *J. Fluids Struct.* (2003) **17**:855–874.

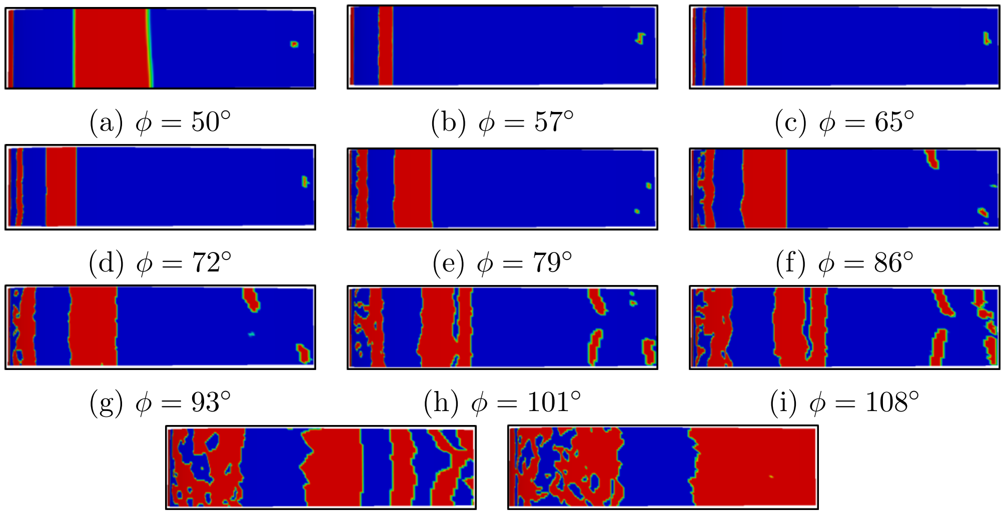

(a) $\phi = 50°$ (b) $\phi = 57°$ (c) $\phi = 65°$

(d) $\phi = 72°$ (e) $\phi = 79°$ (f) $\phi = 86°$

(g) $\phi = 93°$ (h) $\phi = 101°$ (i) $\phi = 108°$

(j) $\phi = 144°$ (k) $\phi = 180°$

Figure 25: Instantaneous spanwise vorticity w_z over the range of ± 30, near the wing suction surface during transition for $Re_c = 5 \times 10^4$, $\alpha = 5°$; $k = 0.94$ and $A/c = 0.5$.

[5] Medjroubi, W., Stoevesandt, B., Carmo, B. and Peinke, J. High-order numerical simulations of the flow around a heaving wing. *Compt Fluids.* (2011) **51**:68–84.

[6] Peinke, J., Stoevesandt, B. and Medjroubi, W. Wake classification of heaving airfoils using spectral/hp element method. *J. Compt Appl Maths.* (2012) **236**:3774–3782.

[7] Winslow, J., Otsuka, H., Govindarajan, B. and Chopra, I. Basic Understanding of Airfoil Characteristics at Low Reynolds Numbers $O(10^4 - 10^5)$. *AIAA J Aircraft.* (2018) **55**:1050-1061.

[8] McAlister, W., Carr, L.W. and McCroskey, W.J. Analysis of the development of dynamic stall based on oscillating airfoil experiment. *Tech. Rep. NASA Tech. Mem.*8382 (1977).

[9] McCroskey, W.J. The phenomenon of dynamic stall. *Tech. Rep. TR 81-A-6. NASA.* (1981).

[10] Choi, J., Colonius, T. and Williams, D. Dynamics and energy extraction of a surging and plunging airfoil at low Reynolds number. *AIAA Journal.* (2013) :2013-0672.

[11] Carr, L.W. Progress in analysis and prediction of dynamic stall. *AIAA J Aircraft.* (1988) **25**:6-17.

[12] Leishman, J. Dynamic stall experiments on the NACA 23012 aerofoil. *J. Expt Fluids.* (1990) **9**:49–58.
[13] Lee, T. and Gerontakos, P. Investigation of flow over over an oscillating airfoil. *J. Fluid Mech.* (2004) **512**:313–341.
[14] Rudmin, D., Benaissa, A. and Poirel, D. Detection of laminar flow separation and transition on a NACA 0012 airfoil using surface hot-films. *J. Fluids Eng.* (2013) **135**:101104–1.
[15] Kim, D.H. and Chang, J.W. Low-Reynolds-number effect on the aerodynamic characteristics of a pitching NACA0012 airfoil. *J. Aero Sci Tech.* (2014) **32**:162–168.
[16] Cleaver, D.J., Gursul, I., Wang, Z. and Calderon, D.E. Lift enhancement through flexibility of plunging wings at low Reynolds numbers. *J. Fluids Struct.* (2016) **64**:27–45.
[17] Chiereghin, N., Gursul, I. and Cleaver, D.J. Unsteady force and flow measurements for plunging finite wing. *AIAA Paper.* (2017) **6**:2017-3127.
[18] Ekaterinaris, J.A. and Menter, F.R. Computation of oscillating airfoil flows with one and two equation turbulence models. *AIAA Journal.* (1994) **32**:2359–65.
[19] Barakos, G.N. and Drikakis, D. Unsteady separated flows over maneuvering lifting surfaces. *Philos. Trans R Soc Lond.* (2000) **358**:3279–91.
[20] Wang, S., Ingham, D.B., Ma, L., Pourkashanian, M. and Tao, Z. Numerical investigations on dynamic stall of low Reynolds number flow around oscillating airfoils. *Compt Fluids.* (2010) **39**:1529–1541.
[21] Wang, L., Li, L. and Fu, S. A comparative study of DES type methods for mild flow separation prediction on a NACA0015 airfoil. *Int J. Num Mthds for Heat and Fluid Flows.* (2017) **27**:2528–2543.
[22] Visbal, M.R. High fidelity simulation of transitional flow past a plunging airfoil. *AIAA Journal.* (2009) **47**:2685–2697.
[23] Andro, J.Y. and Jacquin, L. Frequency effects on the aerodynamic mechanisms of a heaving airfoil in a forward flight configuration. *J. Aero Sci Tech.* (2009) **13**:71–80.
[24] Molina, J., Zhang, X. and Angland, D. On the unsteady motion and stability of a heaving airfoil in ground effect. *Acta Mech Sin.* (2011) **27**:164–178.
[25] Kang, C., Aono, H., Baik, Y.S., Bernal, L.P. and Shyy, W. Fluid dynamics of pitching and plunging flat plates at intermediate Reynolds numbers. *AIAA Journal.* (2013) **51**:315–329.

[26] Franck,J.A. and Breuer, K.S. Unsteady high-lift mechanisms from heaving flat plate simulations. *Int J. Heat and Fluid Flow.* (2017) **67**:230–239.
[27] Kim, Y. and Xie, Z.T. Modelling the effects of freestream turbulence on the dynamic stall of wind turbine blades. *Compt Fluids.* (2016) **129**:53–66.
[28] Ouro, P., Stoesser, T. and Ramirez, L. Effect of blade cambering on the dynamic stall in view of designing vertical axis turbines. *J. Fluids Eng.* (2018) **140**:061104–1.
[29] Guillaud, N., Balarac, G. and Goncalvès, E. Large eddy simulations on a pitching airfoil: Analysis of the reduced frequency influence. *Compt Fluids.* (2018) **161**:1–13.
[30] Inagaki, M., Kondoh, T. and Nagano, Y. A mixed-time-scale SGS model with fixed model-parameters for practical LES. *J. Fluids Eng.* (2005) **127**:1–13.
[31] Nicoud, F. and Ducros, F. Subgrid-scale stress modelling based on the square of the velocity gradient tensor. *J. Flow Turbul. Combust.* (1999) **62**:183–200.
[32] Almutairi , J.H. Large-eddy simulation of flow around an airfoil at low Reynolds number near stall. *PhD thesis.* University of Southampton (2010).
[33] Jasak, H. Error analysis and estimation for the finite volume method with application to fluid flows. *PhD thesis.* Imperial College of Science, Technology and Medicine (1996).
[34] Jasak, H. and Tukovič, Z̃. Automatic mesh motion for the unstructured finite volume method. *Trans FAMENA.* (2004) **30**:1-18.
[35] Chiereghin, N., Gursul, I. and Cleaver, D.J. Unsteady Measurements for a periodically plunging airfoil. *AIAA Paper.* (2017) **7**:2017-0996.
[36] Visbal, M.R. Numerical investigation of deep dynamic stall of a plunging airfoil. *AIAA Journal.* (2011) **49**:2157–2170.
[37] Chiereghin, N., Gursul, I. and Cleaver, D.J. Modelling the unsteady loads of plunging airfoils in attached, light and deep stall conditions. Presentation delivered at the Airbus flight physics distributed research and technology partnership (DiPaRT), Bristol (2017).
[38] Visbal, M.R. and Garmann, D.J. Numerical investigation of spanwise end effects on dynamic stall of a pitching NACA 0012 wing. *AIAA Paper.* (2017) :2017–1481.
[39] Spalart, P.R. and Strelets, M.K. Mechanisms of transition and heat transfer in separation bubble. *J. Fluids Mech.*(2000)**403**:329–349.

[40] Leweke, T. and Williamson, C.H.K. Cooperative elliptic instability of a vortex pair. *J. Fluids Mech.* (1998a) **360**:85–119.
[41] Leweke, T. and Williamson, C.H.K. Three- dimensional instability in wake transition. *Eur. J. Mech. B/Fluids* (1998b) **17**:571–586.
[42] Barkley, D. and Henderson, R.D. Three-dimensional Floquet stability analysis of the wake of a circular cylinder. *J. Fluids Mech.* (1996) **322**:215–241.
[43] Waleffe, F. On the three-dimensional instability of strained vortices. *J. Phys Fluids.* (1990) **A2**:76.
[44] Amiralaei, M.R., Alighanbari, H. and Hashemi, S.M. Numerical modelling of a low Reynolds number plunging airfoil flow field characteristics. *Proc of the Inst of Mech Eng, Part G: J. Aero Eng.* (2012) **227**:1251–1264.